

A Stable, High-Order Time-Stepping Scheme for the Drift-Diffusion Model in Modern Solar Cell Simulation

Jun DU¹ and Jun YAN^{1,*}

¹*Guangdong Basic Research Center of Excellence for Aggregate Science,
School of Science and Engineering, The Chinese University of Hong Kong (Shenzhen),
Longgang, Shenzhen, Guangdong 518172, P. R. China*

This paper presents a one-dimensional transient drift–diffusion simulator for advanced solar cells, integrating a structure-preserving finite-volume spatial discretization with Scharfetter–Gummel–type fluxes and a high-order, L-stable implicit Runge–Kutta (Radau IIA) temporal integrator. The scheme ensures local charge conservation, handles sharp material interfaces, and achieves second-order spatial and fifth-order temporal convergence. Its accuracy is verified against the classical depletion approximation in p – n junction and validated through excellent agreement with the established simulator for an organic photovoltaic device. The framework’s extensibility is demonstrated by incorporating exciton kinetics in organic solar cells, capturing multi-timescale dynamics, and by modeling mobile ions in perovskite solar cells, reproducing characteristic J – V hysteresis without empirical parameters. This work provides a robust, high-order numerical foundation for simulating coupled charge, exciton, and ion transport in next-generation photovoltaic devices.

I. INTRODUCTION

Drift–diffusion (DD) modeling has become a central tool for understanding and optimizing modern solar cells, based on materials ranging from crystalline silicon to organic and perovskite semiconductors. By resolving the coupled evolution of electrostatic potential, electronic carrier densities, and, where relevant, mobile ionic species at the device scale typically in range of several hundreds of nanometers, DD simulations bridge microscopic material parameters (mobilities, recombination coefficients, trap and interfacial state densities) and macroscopic observables such as current–voltage characteristics, power conversion efficiency, and transient response. Foundational textbooks such as Nelson’s *The Physics of Solar Cells* [1] have established the DD framework as the standard continuum description for photovoltaic devices, and it is now routinely used alongside optoelectronic experiments and commercial TCAD tools. For hybrid perovskites in particular, transient optoelectronic measurements combined with DD modeling have been instrumental in confirming the role of ion migration and field screening in current–voltage hysteresis and slow transients [2].

Most solar-cell DD models can be understood as variants of the classical van Roosbroeck system, which couples Poisson’s equation for the electrostatic potential with continuity equations for electrons and holes, supplemented by constitutive relations for drift–diffusion currents and recombination–generation processes [3]. This framework has been rigorously analyzed and extended to include mixed ionic–electronic transport, non-Boltzmann statistics, and sophisticated interface conditions [4]. From the numerical viewpoint, the van Roosbroeck system poses several challenges: it is nonlinear and strongly coupled, it involves small intrinsic length scales such as the Debye

length, and in mixed conductors it contains widely separated time scales associated with electronic carriers, traps, and mobile ions. Any practical solver must therefore cope with stiffness while preserving basic physical properties such as local charge conservation, positivity of carrier densities, and meaningful equilibrium limits over wide parameter ranges.

A variety of spatial discretization strategies have been developed for the drift–diffusion equations. Early device simulators often employed finite-difference schemes on structured grids, while finite-element methods (FEM) have enabled simulations on complex geometries and in multiphysics settings (e.g. coupled electro–optical or degradation models). For one-dimensional or layered photovoltaic structures, however, finite-volume (FV) discretizations have emerged as particularly attractive because they enforce local conservation at the level of control volumes and naturally accommodate material interfaces, steep doping gradients, and discontinuous coefficients. Structure-preserving FV schemes based on Scharfetter–Gummel (SG) type fluxes [5] are widely regarded as the standard for solving drift–diffusion equations: they are exponentially fitted to the local electric field, preserve positivity, and recover the correct thermal equilibrium. Recent work has generalized SG fluxes to degenerate statistics and multicomponent systems and has established discrete entropy/energy dissipation properties for FV schemes applied to perovskite solar cell models [6]. Alternative formulations based on electrochemical potentials and quasi-Fermi potentials, as in Abdel et al. [6], improve conditioning and make thermodynamic structure more explicit. In parallel, Azzouzi et al. have combined DD transport with detailed exciton kinetics for organic solar cells [7], illustrating how complex exciton energy transfer process can be incorporated consistently in continuum descriptions. These studies show that, with suitable discretization schemes, the drift–diffusion framework can be extended to accommodate more complex device physics while maintaining stability and accuracy during long-term

* yanjun@cuhk.edu.cn

simulations, especially under steady-state or equilibrium conditions.

On the software side, several open or semi-open one-dimensional DD codes have become standard tools in the photovoltaic community. IonMonger, introduced by Courtier et al., is an open-source MATLAB-based simulator for planar perovskite solar cells that solves a three-layer (ETL/perovskite/HTL) mixed ionic–electronic model [8]. The governing equations are discretized in space by a second-order finite-element scheme on a graded mesh resolving narrow Debye layers, and temporal integration of the resulting DAE system is delegated to MATLAB’s stiff multistep solver `ode15s`. Importantly, IonMonger explicitly does not use SG-type fluxes, instead relying on a standard FEM discretization tailored to Debye-layer resolution, and in its three-layer formulation only the majority carrier is treated in each transport layer (electrons in the ETL, holes in the HTL). Minority carriers in these layers are not evolved as independent variables, which complicates the treatment of nearly intrinsic or weakly doped transport layers and single-carrier experiments where minority-carrier dynamics in the transport layers are relevant. IonMonger 2.0 extends and refactors the original implementation but retains the MATLAB `ode15s` backbone [9], tying time integration to a proprietary black-box solver and limiting direct experimentation with alternative integrators and linear solvers at the PDE level.

Driftfusion, developed by Calado et al., takes a complementary approach: it provides a flexible MATLAB front-end for general one-dimensional mixed ionic–electronic devices that allows an arbitrary number of layers and up to four mobile species [10]. Spatial and temporal discretization, however, are handled by MATLAB’s built-in PDEPE solver, which implements a finite-difference/method-of-lines scheme for parabolic–elliptic systems. Driftfusion introduces a discrete interlayer interface approach in which properties are graded smoothly across finite-thickness “interface regions” between adjacent layers to encode heterojunction energetics and interface-specific recombination mechanisms. While convenient for defining interface models and avoiding explicit jump conditions (e.g. energy level difference), this effectively inserts fictitious interfacial layers of nonzero thickness. Unless the mesh is carefully controlled, a non-negligible fraction of grid points can be spent resolving these artificial regions rather than the physical bulk layers, which reduces the effective resolution for a given computational cost. As in IonMonger, the underlying flux discretization is based on generic finite differences supplied by PDEPE, rather than on SG-type exponentially fitted FV fluxes designed specifically for drift–diffusion transport.

More recently, broader simulation platforms have emerged that embed DD solvers in multi-scale environments. SolarDesign is an online photovoltaic simulation and design platform that couples DFT-based material calculations, optical modeling, DD-based device simulation, and circuit-level analysis within a unified work-

flow [11]. For the electrical level, SolarDesign employs non-uniform SG spatial discretization, semi-implicit time stepping, and Gummel iteration for the coupled Poisson and current-continuity equations, and incorporates specialized sub-models for tunneling, exciton dynamics, and ion migration. SIMsalabim, by Koopmans et al., is another widely used open-source one-dimensional DD code implemented in Pascal with an emphasis on speed, scriptability, and extensibility [12]. It supports steady-state and transient simulations including illumination, mobile ions, trapping–detrapping, and dielectric mismatch, and is frequently used for parameter extraction and model-based data analysis in perovskite and organic solar cells. Both SolarDesign and SIMsalabim offer rich physics and practical workflows, but their time integration strategies remain within the class of “classical” low-order implicit or semi-implicit schemes; they do not aim at systematically exploring high-order stiff integrators tailored to the structure of the semi-discrete DD system.

In addition to the custom solvers developed, several commercial and open-source simulation tools have been widely used for the modeling of drift–diffusion processes in organic and perovskite solar cells. SETFOS (Fluxim) is a commercial suite for optoelectronic device simulation, in which drift–diffusion transport is coupled with optical field calculations. This combination enables routine evaluation of current–voltage characteristics, power-conversion efficiency, and transient responses in tandem devices, and it has been widely used for device optimization and parameter sensitivity studies in organic photovoltaics and related systems [13], [14]. OghmaNano is a free simulator that also targets drift–diffusion modeling across a broad range of semiconductor devices, including organic and perovskite solar cells. It supports both steady-state and transient calculations and has been employed in multiple studies of organic thin-film devices as a reference implementation [15]. In practice, such tools are often used in parallel with in-house solvers for benchmarking, calibration, and cross-validation.

Despite this substantial progress, most DD simulators for solar cells share two numerical features. First, aside from a few mathematically oriented FV schemes, the majority of production codes rely either on generic finite differences/FEM with fluxes not specifically designed for drift–diffusion, or on SG schemes coupled mainly to first- or second-order temporal discretizations. Second, time integration is almost always delegated to low-order implicit multistep schemes: backward Euler, low-order backward differentiation formulae (BDF), or general stiff solvers such as `ode15s` and PDEPE that internally use variable-order BDF/NDF methods [16]. These methods are robust and easy to use, but long transient simulations (e.g. hysteresis protocols, impedance spectroscopy, or light soaking over many decades in time) often require very small time steps to achieve acceptable accuracy, because the global order of accuracy is low and stringent tolerances are needed when each step entails a large nonlinear solve. High-order implicit Runge–Kutta (IRK) schemes, and in particular

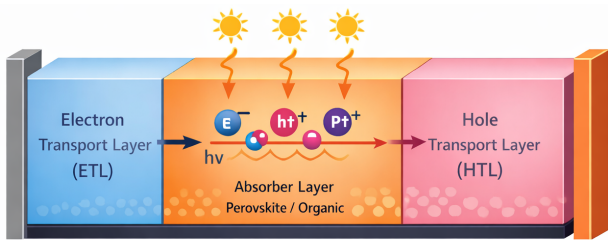


FIG. 1. Schematic of the one-dimensional sandwich-type solar-cell structure considered in this work. The device consists of an electron-transport layer (ETL), an absorber layer (perovskite or organic), and a hole-transport layer (HTL), sandwiched between left (Cathode) and right (Anode) contacts. Material parameters, generation profiles, and boundary conditions can be specified independently in each subregion.

the Radau IIA family, are a natural candidate to address this limitation. Radau IIA methods are algebraically stable, L-stable, and stiffly accurate, making them especially well suited to parabolic and reaction-diffusion type problems where fast modes must be strongly damped [17]. Their higher order convergence (e.g. fifth order for the three-stage Radau IIA scheme) allows a given accuracy to be attained with significantly fewer, larger time steps than first-order backward Euler or low-order BDF, at the price of solving a coupled stage system at each step. Although IRK methods are classical in the ODE/DAE literature and have been used in some fluid and structural dynamics applications, there are few systematic applications of high-order IRK combined with structure-preserving FV/SG discretizations in the context of drift-diffusion modeling for solar cells.

In this work we address this gap by developing a one-dimensional drift-diffusion solar-cell simulator based on a finite-volume discretization with Scharfetter-Gummel-type fluxes for the Poisson and continuity equations, combined with an implicit fifth-order Radau IIA scheme for time integration of the resulting stiff DAE system. Figure 1 illustrates the generic sandwich-type device geometry (ETL/absorber/HTL) considered in this work. The finite-volume formulation ensures local charge conservation, handles heterogeneous multilayer stacks and sharp material interfaces in a natural way, and is compatible with both density-based and potential-based formulations, including mobile ionic species. Building on insights from potential-based and entropy-stable FV schemes [6], our spatial discretization is designed to maintain positivity and asymptotic consistency across strongly inhomogeneous devices. The implicit fifth-order Radau IIA integrator then enables accurate resolution of transients spanning many orders of magnitude in time while keeping the number of nonlinear solutions manageable. In contrast to MATLAB-based frameworks that treat time stepping as a black box, we integrate the IRK stages directly into a tailored nonlinear solution strategy, allowing the reuse of Jacobians and preconditioners across stages and steps and

facilitating tight coupling to the underlying FV structure. Taken together, this space-time discretization is intended to provide a numerically stable, high-order, and independent framework capable of capturing both steady-state and transient behavior of advanced solar-cell architectures, while addressing several of the modeling and algorithmic limitations identified in existing DD simulators.

II. DRIFT DIFFUSION MODEL

A. Basic equations

The drift-diffusion models (Van Roosbroeck's system [3]) are a set of nonlinear equations that comprise continuity equations for electric charge carriers and the Poisson equation for the electrostatic potential of the semiconductor devices. Considering the one dimensional and double-carrier case, the governing equations of the drift diffusion models are as follows:

$$\frac{\partial^2 \phi}{\partial x^2} = -\frac{q}{\epsilon}(p - n + N_D - N_A), \quad (1)$$

$$\frac{\partial n}{\partial t} = -\frac{\partial}{\partial x} \left(\frac{\mathbf{J}_n}{-q} \right) + G - R, \quad (2)$$

$$\frac{\partial p}{\partial t} = -\frac{\partial}{\partial x} \left(\frac{\mathbf{J}_p}{q} \right) + G - R, \quad (3)$$

carrier drift-diffusion fluxes $\mathbf{J}_n, \mathbf{J}_p$ can be expressed by quasi-Fermi levels E_{Fn}, E_{Fp} :

$$\mathbf{J}_n = n\mu_n \frac{\partial E_{Fn}}{\partial x}, \quad \mathbf{J}_p = p\mu_p \frac{\partial E_{Fp}}{\partial x}. \quad (4)$$

Here, we set spatial domain in $[0, L] = \Omega = \Omega_1 \cup \Omega_2 \cdots \cup \Omega_K \subset \mathbb{R}$, where $\Omega_1, \cdots, \Omega_K$ represent different semiconductor material regions (totally K regions), and $t \in [t_0, t_f]$ represents time. The relevant physical parameters are as below:

- ϕ, n, p are unknown variables, represent potential, electron density and hole density, respectively. The electric field is defined by $E = -\partial\phi/\partial x$, and carrier density satisfy Fermi-Dirac distribution $n = N_c F_{1/2}(\eta_e)$ and $p = N_v F_{1/2}(\eta_h)$, where N_c, N_v are effective density of state (eDOS), $F_{1/2}(\eta)$ is 1/2 order Fermi-Dirac integral (numerically, we use Blake-more approximation [18], with $F_{1/2}(\eta) = 1/(e^\eta + \gamma)$ and $\gamma = 0.27$)

$$F_{1/2}(\eta) = \frac{2}{\sqrt{\pi}} \int_0^\infty \frac{\sqrt{x}}{e^{x-\eta} + 1} dx, \quad (5)$$

where $\eta_e = (-q\phi + E_{Fn} - E_c)/k_B T$, $\eta_h = (q\phi - E_{Fp} + E_v)/k_B T$ with charge per electron q , Boltzmann constant k_B and temperature T , E_c and E_v are conduction band and valence band, respectively.

- ϵ the permittivity of a material, is given by $\epsilon = \epsilon_0 \epsilon_r$, where ϵ_0 is the vacuum permittivity and ϵ_r is the relative permittivity.

- N_D and N_A denote the donor concentration and acceptor concentration.
- μ_n and μ_p are the electron and hole mobility, respectively, satisfy the Einstein relation

$$D = \mu V_t, \quad (6)$$

where D is carrier diffusion coefficient, $V_t = \frac{k_B T}{q}$.

- G is generation rate w.r.t. time and space.
- R is recombination rate w.r.t. (n, p) , time and space, e.g., considering Shockley-Read-Hall (SRH) and bimolecular recombination:

$$R = \frac{np - n_i^2}{\tau_p(n + n_1) + \tau_n(p + p_1)} + \beta(np - n_i^2), \quad (7)$$

where τ_n, τ_p are SRH time constants for electrons and holes, n_i is intrinsic density, n_1 and p_1 are parameters that define the dependence of the recombination rate on the trap level E_{trap} , β is the rate constant of bimolecular recombination.

B. Boundary conditions and initial conditions

We set up a mixed boundary condition consisting of ohmic contacts and Schottky contacts, which are mathematically represented as Dirichlet and Robin boundary conditions, respectively:

$$\phi|_{x=0} = 0, \quad (8)$$

$$\phi|_{x=L} = V_{\text{bi}} - V_{\text{app}}(t), \quad (9)$$

$$\mathbf{J}_n|_{x=0} = v_{n,l}(n|_{x=0} - n_{0,l}) \quad (10)$$

$$\mathbf{J}_n|_{x=L} = -v_{n,r}(n|_{x=L} - n_{0,r}) \quad (11)$$

$$\mathbf{J}_p|_{x=0} = -v_{p,l}(p|_{x=0} - p_{0,l}) \quad (12)$$

$$\mathbf{J}_p|_{x=L} = v_{p,r}(p|_{x=L} - p_{0,r}) \quad (13)$$

where V_{bi} is the build-in potential, V_{app} is the applied voltage, $v_{n/p,r/l}$ represent boundary electron recombination velocity on left/right boundary, $n_{0,l/r}$ and $p_{0,l/r}$ are electron and hole density on left/right boundary at equilibrium, given by

$$n_{0,l/r} = N_c F_{1/2} \left(\frac{E_F - E_c}{k_B T} \right), \quad (14)$$

$$p_{0,l/r} = N_v F_{1/2} \left(\frac{E_v - E_F}{k_B T} \right), \quad (15)$$

where E_F is Fermi energy level.

For the system in consistency, we require that the initial guess of (n, p) satisfy charge neutrality condition and equilibrium condition (here we set equilibrium Fermi level E_F at 0)

$$p - n + N_D - N_A = 0, \quad (16)$$

$$E_{\text{Fn}} = E_{\text{Fp}} = 0, \quad (17)$$

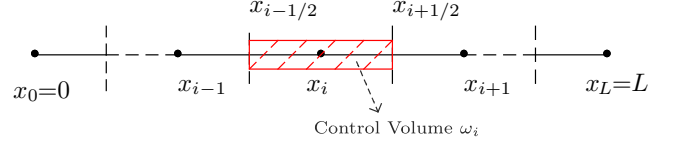


FIG. 2. A schematic of Spatial Discretization.

and assume no electrical field, i.e. the potential $\phi(x) = 0$, for initial guess. For transient problem, the initial condition of transient term $\partial_t y$ (for any unknown variable y regard as y') is obtained by solving system $F(y, y', t, x)$ using newton's method, referring to [19].

III. NUMERICAL METHODS AND ALGORITHMS

A. Spatial mesh

Considering the potential occurrence of large gradients at the boundaries, we apply the *tanh* grid mapping [20] to the subdomain $x \in [0, L_1) \cup (L_1, L_2) \cdots \cup (L_{j-1}, L_j) \cdots \cup (L_{K-1}, L]$, ensuring good resolution at the boundaries:

$$\frac{x_i - L_{j-1}}{|L_j - L_{j-1}|} = \frac{1}{2} \left(\frac{\tanh \left[\xi \left(\frac{2i}{\sum_{i=0}^{N_j} i} - 1 \right) \right]}{\tanh(\xi)} + 1 \right), \quad (18)$$

for $x_i \in \Omega_j$.

where N_j represents node number of the j th material, ξ represents the degree to which points are concentrated near the boundaries (generally let $\xi = 5$). For convenience, the ghost point x_0 and x_N are set to represent boundary condition, so the mesh consists of $\sum_{j=0}^K N_j + 2$ nodes. For these subintervals, their control volume are defined as $\omega_i^- = x_i - x_{i-1/2}$, $\omega_i^+ = x_{i+1/2} - x_i$ and $\omega_i = \omega_i^+ + \omega_i^-$, as shown in Figure 2.

B. Nondimensionalisation

We introduce dimensionless variables (denoted by a hat) by normalizing each physical quantity with its characteristic scale:

$$\begin{aligned} \hat{x} &= \frac{x}{L}, & \hat{t} &= \frac{t}{\tau}, & \hat{\phi} &= \frac{\phi}{V_t}, \\ \hat{n} &= \frac{n}{N_0}, & \hat{p} &= \frac{p}{N_0}, & \hat{N}_D &= \frac{N_D}{N_0}, \\ \hat{N}_A &= \frac{N_A}{N_0}, & \hat{\mathbf{J}}_n &= \frac{\mathbf{J}_n}{qG_0 b}, & \hat{\mathbf{J}}_p &= \frac{\mathbf{J}_p}{qG_0 b}, \\ \hat{G} &= \frac{G}{G_0}, & \hat{R} &= \frac{R}{G_0}, & \hat{v} &= \frac{vN_D}{G_0 b}, \\ \hat{E}_{\text{Fn}} &= \frac{E_{\text{Fn}}}{k_B T}, & \hat{E}_{\text{Fp}} &= \frac{E_{\text{Fp}}}{k_B T}. \end{aligned} \quad (19)$$

$$N_0 = \|N_D, N_A\|_{\max}, \quad L_D = \sqrt{\frac{V_t \|\varepsilon\|_{\max}}{q N_0}},$$

$$G_0 = \frac{N_0 \cdot \|D_n, D_p\|_{\max}}{L^2}, \quad \tau = \frac{N_0}{G_0}. \quad (20)$$

$$\lambda = \frac{L_D}{L}, \quad \kappa_n = \frac{D_n N_0}{G_0 L^2}, \quad \kappa_p = \frac{D_p N_0}{G_0 L^2}. \quad (21)$$

where L_D is so-called Debye length. From these scales we obtain the dimensionless parameters then (after dropping the hats on the parameters and variables) equations can be rewritten as

$$0 = -\lambda^2 \frac{\partial \mathbf{E}}{\partial x} + p - n + N_D - N_A, \quad \mathbf{E} = -\frac{\partial \phi}{\partial x}, \quad (22)$$

$$\frac{\partial n}{\partial t} = \frac{\partial \mathbf{J}_n}{\partial x} + G - R, \quad \mathbf{J}_n = \kappa_n n \frac{\partial E_{Fn}}{\partial x}, \quad (23)$$

$$\frac{\partial p}{\partial t} = -\frac{\partial \mathbf{J}_p}{\partial x} + G - R, \quad \mathbf{J}_p = \kappa_p p \frac{\partial E_{Fp}}{\partial x}. \quad (24)$$

Notice that the Debye length is much smaller than the physical characteristic length, there is a small parameter λ^2 in front of the electric potential term in the Poisson equation Eq.(22), which will result in a *singular perturbation* problem [21], [22], thus the *tanh* grid mapping Eq.(18) is necessary.

C. Finite volume scheme

The general form of time dependent nonlinear transport-reaction problems with transient term $\partial_t u$, flux term \mathbf{F} , reaction term $r(u)$ and source term f :

$$\partial_t u = \nabla \cdot \mathbf{F} + r(u) + f, \quad (25)$$

where u is unknown function. Apply the Gauss theorem for the divergence term, we have

$$\int_{\Omega} \nabla \cdot \mathbf{F} d\Omega = \oint_{\partial\Omega} \mathbf{F} \cdot d\mathbf{n} = \sum_k \mathbf{F}_{ik} d_{ik}, \quad (26)$$

where $\partial\Omega$ is the boundary, \mathbf{n} is direction vector, \mathbf{F}_{ik} is the midpoint flow density on the edge (i, k) whose direction is from vertex i to vertex k , d_{ik} is the length of the side perpendicular to the opposite side (i, k) on the polygon Ω . In one dimension case, the transport equation has the form

$$\int \frac{\partial s(u)}{\partial t} d\omega_i = \sum_k \mathbf{F}_{ik} d_{ik} + \int (r(u) + f) d\omega_i, \quad (27)$$

the integral of the flux divergence at the boundary of the control volume is

$$\sum_k \mathbf{F}_{ik} d_{ik} = \mathbf{F}_{i+1/2} - \mathbf{F}_{i-1/2}. \quad (28)$$

For simplicity, we employ a piecewise linear scheme, assuming that the transient and source terms are locally linear within each control volume, and use Simpson's method[23] to approximate reaction term, this approach then for each control volume gives:

$$\omega_i \frac{\partial s(u)}{\partial t} = \mathbf{F}_{i+1/2} - \mathbf{F}_{i-1/2} + \mathcal{S}_i[r(u)] + \omega_i f_i, \quad (29)$$

where an operator \mathcal{S}_i is defined as $\mathcal{S}_i[r(u)] := \frac{\omega_i}{6} [r(u_{i-1/2}) + 4r(u_i) + r(u_{i+1/2})]$, furthermore, by using average approximation $r(u_{i+1/2}) \approx \frac{r(u_i) + r(u_{i+1})}{2}$ of reaction term (recombinations Eq.(7) are not exceeding 2 order), then Simpson integral operator turns to $\mathcal{S}_i[r(u)] = [\frac{1}{12}r(u_{i-1}) + \frac{5}{6}r(u_i) + \frac{1}{12}r(u_{i+1})] \omega_i$.

The finite-volume method (FVM) ensures that the physical quantities obey the conservation laws in each control volume. To express the the discretized system of equations in a concise way, we introduce the difference and average operator for a generic dependent variable u :

$$D_x u_{i+1/2} := \frac{u_{i+1} - u_i}{\Delta_{i+1/2}}, \quad (30)$$

$$A_x u_{i+1/2} := \frac{u_{i+1} + u_i}{2}, \quad (31)$$

where $\Delta_{i+1/2} = x_{i+1} - x_i$. For electrical field, we use finite difference approximation $\mathbf{E}_{i+1/2} \approx -D_x \phi_{i+1/2}$; for electrons/holes fluxes, we employ the Scharfetter Gummel [5] scheme (also known as Il'in [24], Allen-Southwell [25]) which is obtained by solving a local boundary value problem (BVP) across the intervals or can be explained by a kind of general harmonic average, e.g., by defining $\gamma_e = \ln \frac{F_{1/2}(\eta_e)}{\exp(\eta_e)} - E_c + \ln N_c$, we have $n \frac{\partial E_{Fn}}{\partial x} = \exp(\phi + \gamma_e) \frac{\partial \exp(E_{Fn})}{\partial x}$, which leads to $\mathbf{J}_{n,i+1/2} \approx A_x \kappa_{n,i+1/2} \frac{\gamma'_{i+1} - \gamma'_i}{\int_{\gamma'_i}^{\gamma'_{i+1}} \exp(\gamma') dx} \frac{\exp(E_{Fn,i+1}) - \exp(E_{Fn,i})}{\Delta_{i+1/2}}$. Assuming $\gamma' = \phi + \gamma_e$ changes linearly within the subinterval $[x_i, x_{i+1}]$, one can obtain

$$\mathbf{J}_{n,i+1/2} = \frac{A_x \kappa_{n,i+1/2}}{\Delta_{i+1/2}} [B(-z_n) n_{i+1} - B(z_n) n_i], \quad (32)$$

where $z_n = (E_{Fn,i+1} - E_{Fn,i}) - \ln \frac{F_{1/2}(\eta_{e,i+1})}{F_{1/2}(\eta_{e,i})} - \ln \left(\frac{N_{c,i+1}}{N_{c,i}} \right)$, and $B(x) = \frac{x}{e^x - 1}$ is Bernoulli function. Similarly, for hole fluxes,

$$\mathbf{J}_{p,i+1/2} = \frac{-A_x \kappa_{p,i+1/2}}{\Delta_{i+1/2}} [B(z_p) p_{i+1} - B(-z_p) p_i], \quad (33)$$

where $z_p = -(E_{Fp,i+1} - E_{Fp,i}) - \ln \frac{F_{1/2}(\eta_{h,i+1})}{F_{1/2}(\eta_{h,i})} - \ln \frac{N_{v,i+1}}{N_{v,i}}$.

Lastly, the semi-discrete system for (22)-(24) can be regard as differential algebraic equations (DAE) in terms of time variable t :

$$0 = \phi_0, \quad (34)$$

$$0 = -\lambda^2(\mathbf{E}_{i+1/2} - \mathbf{E}_{i-1/2}) + \omega_i(p_i - n_i + N_{D,i} - N_{A,i}) \quad (35)$$

for $i = 1, 2, \dots, N - 1,$

$$0 = \phi_N + V_{\text{app}}(t) - V_{\text{bi}}, \quad (36)$$

$$0 = \mathbf{J}_{n,1/2} - v_{n,l}(n_0 - n_{0,l}) \quad (37)$$

$$\omega_i \frac{dn_i}{dt} = \mathbf{J}_{n,i+1/2} - \mathbf{J}_{n,i-1/2} + \omega_i G_i - \mathcal{S}_i R \quad (38)$$

for $i = 1, 2, \dots, N - 1,$

$$0 = -\mathbf{J}_{n,N-1/2} - v_{n,r}(n_N - n_{0,r}), \quad (39)$$

$$0 = -\mathbf{J}_{p,1/2} - v_{p,l}(p_0 - p_{0,l}), \quad (40)$$

$$\omega_i \frac{dp_i}{dt} = -(\mathbf{J}_{p,i+1/2} - \mathbf{J}_{p,i-1/2}) + \omega_i G_i - \mathcal{S}_i R \quad (41)$$

for $i = 1, 2, \dots, N - 1,$

$$0 = \mathbf{J}_{p,N-1/2} - v_{p,r}(p_N - p_{0,r}). \quad (42)$$

D. Dynamics in Solar Cells

Beyond purely electronic transport, many modern solar-cell architectures involve additional internal degrees of freedom such as excitonic populations in organic blends or mobile ionic defects in metal-halide perovskites. In the present framework, these processes are treated in a way that is fully consistent with the nondimensionalization and discretization introduced in Sections III B and III C. For organic solar cells, the local LE/CT exciton kinetics are described by zero-dimensional rate equations at each spatial grid point, see Eqs.(43)–(44), which enter the discretized system as stiff reaction terms coupled to the electronic carrier densities n and p [7]. For perovskite solar cells, mobile ionic vacancies obey a one-dimensional conservation law with drift-diffusion flux \mathbf{J}_P , so that Eq.(47)

which is discretized by the same finite-volume machinery and SG-type fluxes as the electronic currents. After rescaling with the global characteristic length and time scales, all additional variables (excitons, ions) simply augment the semi-discrete DAE system in Eqs.(34)–(42) and are advanced in time by the common fifth-order Radau IIA integrator. This highlights that the proposed numerical framework is not tied to a specific device physics, but can accommodate new dynamic sub-models in a modular way.

1. Kinetics of excitons

For organic solar cells (OSC), we mainly consider the local exciton (LE) state and the interfacial charge transfer (CT) state using zero-dimensional rate equations, described by [7]:

$$\frac{\partial[\text{LE}]}{\partial t} = G_{\text{opt}} - k_{\text{trans}}^{\text{LE} \rightarrow \text{CT}}[\text{LE}] + k_{\text{trans}}^{\text{CT} \rightarrow \text{LE}}[\text{CT}] - k_{\text{rec}}^{\text{LE}}([\text{LE}] - [\text{LE}]_0), \quad (43)$$

$$\frac{\partial[\text{CT}]}{\partial t} = k_{\text{trans}}^{\text{LE} \rightarrow \text{CT}}[\text{LE}] - k_{\text{diss}}^{\text{CT} \rightarrow \text{CS}}[\text{CT}] - k_{\text{trans}}^{\text{CT} \rightarrow \text{LE}}[\text{CT}] - k_{\text{rec}}^{\text{CT}}([\text{CT}] - [\text{CT}]_0) + B_{\text{for}}^{\text{CS} \rightarrow \text{CT}} np, \quad (44)$$

where G_{opt} is the generation rate obtained from optical model, k_{trans} is the constant transfer rate between LE and CT states, k_{diss} is constant dissociation rate that CT state contribute the free charge carriers, k_{rec} the constant rate for LE and CT state recombination, B_{for} the constant rate of formation of a CT state from free charge carriers, $[\text{LE}]_0/[\text{CT}]_0$ is the equilibrium exciton density for the lowest LE and CT state, respectively. Coupled with drift-

diffusion model, the continuity equations of free electrons and holes turns to describe charge separated (CS) state:

$$\frac{\partial n}{\partial t} = -\frac{\partial}{\partial x} \left(\frac{\mathbf{J}_n}{-q} \right) + k_{\text{diss}}^{\text{CT} \rightarrow \text{CS}}[\text{CT}] - B_{\text{for}}^{\text{CS} \rightarrow \text{CT}} np \quad (45)$$

$$\frac{\partial p}{\partial t} = -\frac{\partial}{\partial x} \left(\frac{\mathbf{J}_p}{q} \right) + k_{\text{diss}}^{\text{CT} \rightarrow \text{CS}}[\text{CT}] - B_{\text{for}}^{\text{CS} \rightarrow \text{CT}} np. \quad (46)$$

Figure 3 schematically shows the interconversion be-

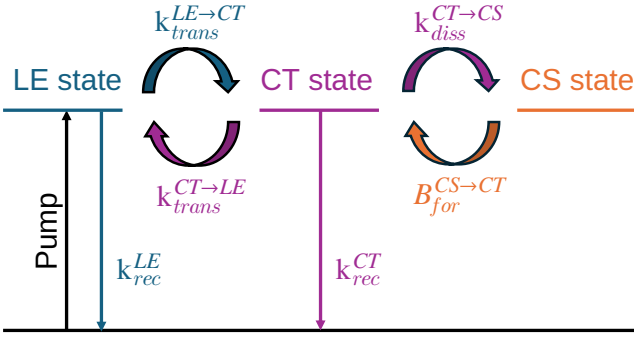


FIG. 3. Schematic of LE-CT-CS state kinetics.

tween LE and CT states, CT dissociation to the charge-separated (CS) state and the reverse back-formation, together with radiative/non-radiative loss channels and photoexcitation (pump).

2. Dynamics of mobile ionic vacancies

For perovskite solar cells (PSC), the conservation of positively-charged anion vacancies P takes the form [20]:

$$\frac{\partial P}{\partial t} = -\frac{\partial \mathbf{J}_P}{\partial x}, \quad (47)$$

with drift and diffusion current due to ionic motion:

$$\mathbf{J}_P = -D_+ \left(\frac{\partial P}{\partial x} + \frac{P}{V_t} \frac{\partial \phi}{\partial x} \right),$$

where D_+ represents anion vacancy diffusion coefficient.

Poisson's equation in perovskite layer turns to:

$$\frac{\partial^2 \phi}{\partial x^2} = -\frac{q}{\epsilon} (P - N_I + p - n),$$

where N_I is the uniform density of cation vacancies (for satisfying the global charge neutrality).

E. Time stepping

The problem to be solved can now be written in the form

$$M \frac{dy}{dt} = f(t, y), \quad (48)$$

where M is mass matrix, y is solution vector contains $y = [\phi, n, p]$ and $f(t, y)$ represent right-hand-side (rhs) of equations at t . Due to the *stiffness* of the system, the time-stepping algorithm must be L stable [26]. Compared to the traditional Backward Euler (BE, 1st-order accuracy) and Backward Differentiation Formula 2 (BDF2, 2nd-order accuracy) algorithms, we choose the 5th-order Implicit Runge-Kutta method from the Radau IIA family, which maintains 5th-order accuracy

TABLE I. Butcher table for Radau IIA.

$\frac{4-\sqrt{6}}{10}$	$\frac{88-7\sqrt{6}}{360}$	$\frac{296-169\sqrt{6}}{1800}$	$\frac{-2+3\sqrt{6}}{225}$
$\frac{4+\sqrt{6}}{10}$	$\frac{296+169\sqrt{6}}{1800}$	$\frac{88+7\sqrt{6}}{360}$	$\frac{-2-3\sqrt{6}}{225}$
1	$\frac{16-\sqrt{6}}{36}$	$\frac{16+\sqrt{6}}{36}$	$\frac{1}{9}$
	$\frac{16-\sqrt{6}}{36}$	$\frac{16+\sqrt{6}}{36}$	$\frac{1}{9}$

while ensuring L-stability. The implementation of Radau IIA is based on modifications to the Radau solver in the `scipy.integrate` subpackage [27], with reference to [28], to achieve the numerical solution of differential algebraic equation.

For an ordinary differential equation (ODE) problem $\frac{dy}{dt} = f(t, y)$, the updated formula from a time step t_n to $t_{n+1} = t_n + h$ is [29]

$$y_{n+1} = y_n + h \sum_{i=1}^s b_i K_i, \quad (49)$$

$$K_i = f(t_n + c_i h, Y_i), i = 1, 2, \dots, s \quad (50)$$

where internal stages are evaluated at $t + c_i h$ with fixed nodes c_i , $Y_i = y_n + h \sum_{j=1}^s a_{ij} K_j$ is i -th stage states. The s -stage Radau IIA method can achieve an accuracy of order $2s - 1$, 3-stage Butcher table is as follows [30].

For DAE, with stage states Y_i and stage derivatives $K_i \approx \dot{y}(t + c_i h)$, the collocation equations are

$$MK_i = f(t_n + c_i h, Y_i), i = 1, 2, 3. \quad (51)$$

We work with stage displacements $Z_i := h \sum_j a_{ij} K_j$ and stack them as $Z \in \mathbb{R}^{3 \times n}$. A simplified Newton iteration (Jacobian $J = \partial f / \partial y$ frozen per step, and numerical differentiation $\frac{df}{dx} = \lim_{h \rightarrow 0} \frac{f(x+h) - f(x)}{h}$ is use to calculate the jacobian matrix [31]) would yield a $3n \times 3n$ block system

$$(I_3 \otimes M - hA \otimes J) \Delta K = -\mathcal{R}, \quad (52)$$

where I_3 is 3×3 unit matrix, $A = [a_{11}, \dots; \dots; \dots, a_{33}]$,

$$\mathcal{R} = \begin{pmatrix} MK_1 - f(t_1 + c_1 h, Y_1) \\ MK_2 - f(t_2 + c_2 h, Y_2) \\ MK_3 - f(t_3 + c_3 h, Y_3) \end{pmatrix}. \quad (53)$$

The implementation diagonalizes the 3×3 Butcher matrix once,

$$A = T \Lambda T^{-1}, \quad (54)$$

where $\Lambda = \text{diag}(\lambda_{\text{real}}, \lambda, \bar{\lambda})$ with one real eigenvalue and

a complex-conjugate pair, T is fixed change of basis:

$$\begin{aligned}\lambda_{\text{real}} &= \frac{1}{3 + 3^{2/3} - 3^{1/3}} := \frac{1}{\mu_{\text{real}}}, \\ \lambda, \bar{\lambda} &= \frac{1}{3 + \frac{1}{2}(3^{1/3} - 3^{2/3}) \mp \frac{i}{2}(3^{5/6} + 3^{7/6})} := \frac{1}{\mu_\lambda}, \frac{1}{\mu_{\bar{\lambda}}}, \\ \Lambda &= \begin{pmatrix} \lambda_{\text{real}} & 0 & 0 \\ 0 & \lambda & 0 \\ 0 & 0 & \bar{\lambda} \end{pmatrix}, \\ T &= \begin{pmatrix} \frac{3}{32} - \frac{\sqrt{6}}{48} & -\frac{3}{32} - \frac{\sqrt{6}}{48} & \frac{1}{16} \\ \frac{1}{4} & \frac{1}{4} & -\frac{3}{8} \\ 1 & 1 & 0 \end{pmatrix}, \\ T^{-1} &= \begin{pmatrix} \frac{16}{3} & -\frac{4}{3} & \frac{8}{3} \\ -\frac{16}{3} & \frac{4}{3} & -\frac{8}{3} \\ \frac{8}{3} & -\frac{20}{3} & \frac{8}{3} \end{pmatrix}.\end{aligned}\quad (55)$$

Changes stage variables $W = T^{-1}Z$ (so $Z = TW$), $W = W_0 + (W_1 + iW_2)$, in these coordinates, the Newton system decouples into three $n \times n$ systems:

$$h_s \left(\frac{\mu_\ell}{h} M - J \right) \Delta W_\ell = r_\ell, \quad (56)$$

where

$$\mu_\ell = 1/\lambda_\ell, \quad \ell \in \{\text{real}, \lambda, \bar{\lambda}\}, \quad (57)$$

$$r_{\text{real}} = S \left(F^\top T_{\text{real}} - \frac{\mu_{\text{real}}}{h} M W_0 \right), \quad (58)$$

$$r_{\text{complex}} = S \left(F^\top T_{\text{complex}} - \frac{\mu_{\text{complex}}}{h} M (W_1 + iW_2) \right), \quad (59)$$

$$F = [f(t_1 + c_1 h, Y_1); f(t_2 + c_2 h, Y_2); f(t_3 + c_3 h, Y_3)]. \quad (60)$$

and h_s, S is diagonal scaling:

$$S = \text{diag}(h_s). \quad (61)$$

Because two eigenvalues form a complex-conjugate pair, only two LU factorizations are needed per step: one real and one complex; the complex update is split into real/imaginary parts and mapped back by T .

After Newton converges, an embedded order-3 error is computed by reusing the real LU:

$$\left(\frac{\mu_{\text{real}}}{h} M - J \right) e = f(t_n, y_n) + \frac{1}{h} M Z_E, \quad (62)$$

with a fixed linear combination Z_E of stages. The scaled norm $\|e\|_{\text{sc}}$ is compared to 1 (optional handling of algebraic components: scale/zero in the norm). If $\|e\|_{\text{sc}} \leq 1$ the step is accepted, else rejected.

There is one step size h per step. A *Gustafsson*-style predictor controls it:

$$h_{n+1} = h_n \times \left(\frac{\text{tol}}{\text{error}} \right)^{1/(p+1)}, \quad (63)$$

On acceptance, we deal next step h_{n+1} with

$$h_{n+1} = h_n \times \varrho_f \quad (64)$$

where

$$\varrho_f = \min\{\varrho_{\text{max}}, \varpi \cdot \varrho\},$$

on rejection, we use

$$\varrho_f = \max\{\varrho_{\text{min}}, \varpi \cdot \varrho\} \quad (65)$$

to renew recent time step $h_n = h_n \times \varrho_f$, where ϱ_f is the time updating factor, calculated by factor ϱ and safety factor ϖ .

ϱ is defined by a prediction multiplier

$$\varrho = \min \left\{ 1, \frac{h_n}{h_{n-1}} \times \left(\frac{\text{error}_{n-1}}{\text{error}_n} \right)^{1/4} \right\} \cdot \text{error}^{-1/4}, \quad (66)$$

and ϖ defined w.r.t. newton iteration step:

$$\varpi = 0.9 \times \frac{2 \times k_{\text{max}} + 1}{2 \times k_{\text{max}} + k}, \quad (67)$$

where k_{max} is the maximum newton step we expect.

The adaptive Radau IIA stepping procedure used in our implementation is summarized in Algorithm 1.

IV. RESULTS AND VERIFICATION

A. Spatial convergence

Due to non-uniform mesh established, we use the representative mesh size $h = \frac{L}{N}$ (except ghost points) to measure spatial step. Because the exact solution is not available, a reference solution is computed on a very fine grid with $N^{\text{ref}} = 3200$, and $N \in \{50, 100, 200, 400, 800, 1600\}$ for each coarser grid. On the non-uniform grid we define the discrete L^2 -error by the trapezoidal rule

$$E_u(h) = \left(\sum_{i=1}^N \omega_i |u_h(x_i) - u^{\text{ref}}(x_i)|^2 \right)^{1/2}, \quad (68)$$

where ω_i are the standard trapezoidal weights (control volume) built from the local mesh widths, and only interior nodes are included in the sum.

Figure 4 shows L^2 error $E_u(h)$ versus h in log-log scale for $u = P, \phi, n, p$ yields straight lines with slopes close to two, this demonstrates that the proposed spatial discretization is globally *second-order accurate* for all four variables.

B. Temporal convergence

The steps are non-uniform because adaptive time stepping controlled by relative and absolute tolerances $rtol$

Algorithm 1: Adaptive Radau IIA step with frozen Jacobian

Input: Current state (t, y) , step size h , mass matrix M , frozen Jacobian J

Data: $\text{Tol}_{\text{newton}} = 10^{-3}$, $k_{\text{max}} = 6$, $\varrho_{\text{max}} = 10$, $\varrho_{\text{min}} = 0.2$

repeat

if h is too small **then**

 | fail

end

 Compute $t_i = t + c_i h$ and initialize $Z_0 = 0$ (or extrapolate from dense output)

 Build $H_{\text{real}} = h_{\text{scaled}}((\mu_{\text{real}}/h)M - J)$ and

$H_{\text{cplx}} = h_{\text{scaled}}((\mu_{\text{cplx}}/h)M - J)$

 Factorize $\text{LU}_{\text{real}} = \text{LU}(H_{\text{real}})$ and

$\text{LU}_{\text{cplx}} = \text{LU}(H_{\text{cplx}})$

 Set $W = T^{-1}Z_0$

for $k = 1, \dots, k_{\text{max}}$ **do**

 Evaluate $F_i = f(t_i, y + Z_i)$

 Form $r_{\text{real}} = S(F^{\top}T_{\text{real}}^{-1} - (\mu_{\text{real}}/h)MW_0)$

 Form

$r_{\text{cplx}} = S(F^{\top}T_{\text{cplx}}^{-1} - (\mu_{\text{cplx}}/h)M(W_1 + iW_2))$

 Solve $\Delta W_0 = \text{solve}(\text{LU}_{\text{real}}, r_{\text{real}})$

 Solve $\Delta(W_1 + iW_2) = \text{solve}(\text{LU}_{\text{cplx}}, r_{\text{cplx}})$

 Update $W \leftarrow W + \Delta W$ and $Z \leftarrow TW$

if $\|\Delta W\|_{\text{scaled}} < \text{Tol}_{\text{newton}}$ **then**

 | break

end

end

if Newton iteration failed **then**

 | $h \leftarrow \max\{\varrho_{\text{min}}, \varpi \cdot \varrho\}h$

 | continue

end

 Compute the embedded error estimate

$e = \text{solve}(\text{LU}_{\text{real}}, f(t, y) + (1/h)MZ_E)$

if $\|e\|_{\text{sc}} \leq 1$ **then**

 | Accept the step: $y \leftarrow y + h \sum b_i K_i(Z)$ and

$t \leftarrow t + h$

 | Set $h_{\text{next}} \leftarrow \min\{\varrho_{\text{max}}, \varpi \cdot \varrho\}h$ and return

end

$h \leftarrow \max\{\varrho_{\text{min}}, \varpi \cdot \varrho\}h$

until step accepted

and $atol$ via *Gustafsson*-style predictor. Thus, we characterize the temporal resolution by an *effective time-step size*. Let $\{t_n\}_{n=0}^M$ be the internal time grid produced by the solver during the second stage, and define

$$\Delta t^{\text{eff}} = \frac{t_M - t_0}{M}, \quad (69)$$

where M is the number of internal steps. We use a very tight tolerance pair ($rtol = 10^{-6}$ and $atol = 10^{-9}$) as reference solution and a sequence of runs are performed for decreasing tolerances $rtol \in \{10^{-2}, 5 \times 10^{-3}, 2.5 \times 10^{-3}, \dots, 3.90625 \times 10^{-5}\}$ with $atol = 10^{-3} \times rtol$, which computed on the same spatial grid ($N = 200$) and results in a corresponding sequence of decreasing effective time stepsizes Δt^{eff} . For each run with a given Δt^{eff} we then measure, at the final time T , the temporal error in the

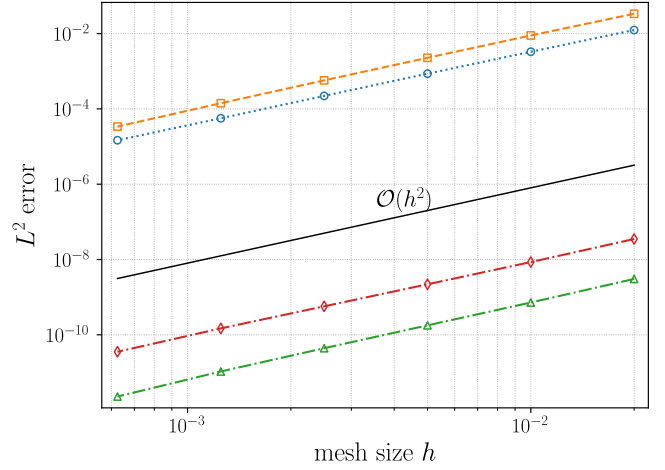


FIG. 4. L^2 error versus mesh size h for P (blue), ϕ (orange), n (green), and p (red), with $\mathcal{O}(h^2)$ reference line (black).

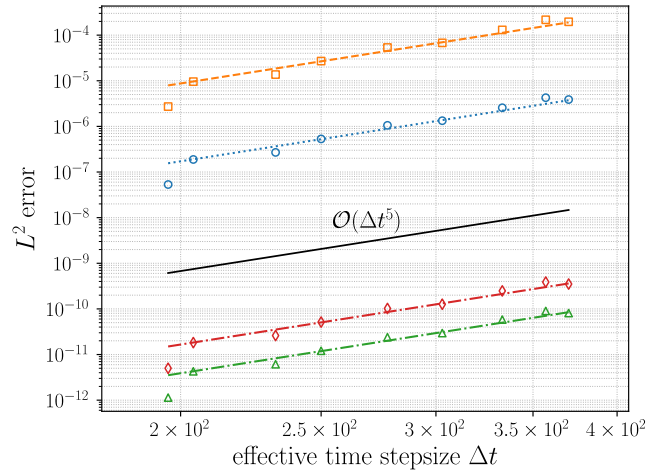


FIG. 5. L^2 error versus effective time stepsize Δt for P (blue), ϕ (orange), n (green), and p (red), with $\mathcal{O}(\Delta t^5)$ reference line (black).

spatial L^2 ,

$$E_u(\Delta t^{\text{eff}}) = \left(\sum_{i=1}^N \omega_i |u_h(x_i, T) - u^{\text{ref}}(x_i, T)|^2 \right)^{1/2}, \quad (70)$$

where the quadrature weights ω_i are the same trapezoidal weights as in the spatial convergence study. Figure 5 plots L^2 error $E_u(\Delta t^{\text{eff}})$ versus Δt^{eff} in log-log scale together with a reference line of slope five, corresponding to $\mathcal{O}(\Delta t^5)$.

The numerical results show that, as the effective time stepsize Δt decreases, the L^2 error for all components P , ϕ , n , and p decays along straight lines that are essentially parallel to the reference curve $\mathcal{O}(\Delta t^5)$ over a wide intermediate range of Δt , which confirms the expected *fifth-order temporal accuracy* of the Radau scheme for this problem. For the largest stepsizes the curves deviate slightly from

this slope, indicating pre-asymptotic behavior before the leading Δt^5 term dominates; for sufficiently small step-sizes one would similarly expect a departure from the ideal Δt^5 scaling once the temporal error becomes comparable to spatial and algebraic errors, although this regime is not yet pronounced in the present simulations.

C. Verification on a p - n junction

As a first steady-state test we consider an abrupt, symmetric p - n junction of total length $L = 400$ nm. The structure consists of an n -type region of thickness $L_n = 200$ nm followed by a p -type region of the same thickness. The donor and acceptor densities are $N_D = N_A = 2.9 \times 10^{22} \text{ m}^{-3}$, the intrinsic carrier concentration is $n_i = 3.5 \times 10^{16} \text{ m}^{-3}$, and the temperature is $T = 298 \text{ K}$, so that the thermal voltage is $V_t = k_B T / q \approx 2.57 \times 10^{-2} \text{ V}$. The geometric interface at which the doping changes from N_D to N_A is referred to as the metallurgical junction and is located at $x_j = L_n$.

For an abrupt p - n junction, the classical depletion approximation predicts the built-in voltage

$$V_{\text{bi}} = V_t \ln \left(\frac{N_D N_A}{n_i^2} \right), \quad (71)$$

and the depletion widths in the n - and p -regions

$$W_n = \sqrt{\frac{2\varepsilon_s}{q} \frac{V_{\text{bi}} N_A}{N_D(N_D + N_A)}}, \quad (72)$$

$$W_p = \sqrt{\frac{2\varepsilon_s}{q} \frac{V_{\text{bi}} N_D}{N_A(N_D + N_A)}}.$$

where ε_s is the semiconductor permittivity. With the above parameters we obtain $V_{\text{bi}} \approx 0.700 \text{ V}$ and $W_n \approx W_p \approx 73.0 \text{ nm}$, so that the total theoretical depletion width is $W_{\text{th}} = W_n + W_p \approx 146.0 \text{ nm}$.

Let $x' = x - x_j$ be the coordinate with origin at the metallurgical junction. Within the depletion region $-W_n \leq x' \leq W_p$, the depletion approximation assumes that only ionized dopants contribute to the space charge. The electrostatic potential (referenced to its value ϕ_L in the left neutral region) is then

$$\phi_{\text{dep}}(x) - \phi_L = -\frac{qN_D}{2\varepsilon_s} (x' + W_n)^2, \quad -W_n \leq x' \leq 0,$$

$$\phi_{\text{dep}}(x) - \phi_L = -\frac{qN_D W_n^2}{2\varepsilon_s} + \frac{qN_A}{2\varepsilon_s} [(x' - W_p)^2 - W_p^2], \quad 0 \leq x' \leq W_p. \quad (73)$$

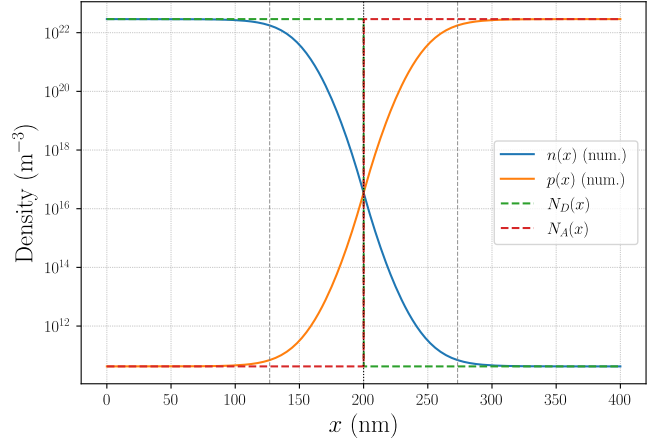


FIG. 6. Equilibrium carrier and doping profiles for the abrupt p - n junction. Solid lines show the numerical electron and hole densities $n(x)$ and $p(x)$; dashed lines indicate the ionized donor and acceptor concentrations $N_D(x)$ and $N_A(x)$. The vertical dotted line marks the metallurgical junction, and the grey dashed lines indicate the depletion edges obtained from the majority-carrier criterion with $\eta = 0.67$.

and the electric field is piecewise linear,

$$E_{\text{dep}}(x) = -\frac{d\phi_{\text{dep}}}{dx} = \begin{cases} \frac{qN_D}{\varepsilon_s} (x' + W_n), & -W_n \leq x' \leq 0, \\ \frac{qN_A}{\varepsilon_s} (W_p - x'), & 0 \leq x' \leq W_p, \\ 0, & |x'| > W_{n,p}. \end{cases} \quad (74)$$

From the numerical drift-diffusion solution we reconstruct the dimensional carrier profiles $n(x)$, $p(x)$ and potential $\phi(x)$. To define a depletion width from the numerical data, we use a majority-carrier threshold criterion. Denoting by x_j the metallurgical junction, we set

$$r_n(x) = \frac{n(x)}{N_D(x)}, \quad x < x_j; \quad (75)$$

$$r_p(x) = \frac{p(x)}{N_A(x)}, \quad x > x_j, \quad (76)$$

and, for a given threshold $\eta \in (0, 1)$,

$$x_n^{\text{num}} = \min\{x < x_j : r_n(x) \leq \eta\}, \quad (77)$$

$$x_p^{\text{num}} = \max\{x > x_j : r_p(x) \leq \eta\}.$$

with numerical depletion width

$$W_{\text{dep}}^{\text{num}} = x_p^{\text{num}} - x_n^{\text{num}}. \quad (78)$$

In this work we choose $\eta = 0.67$. We have verified that the extracted width varies only weakly when η is varied

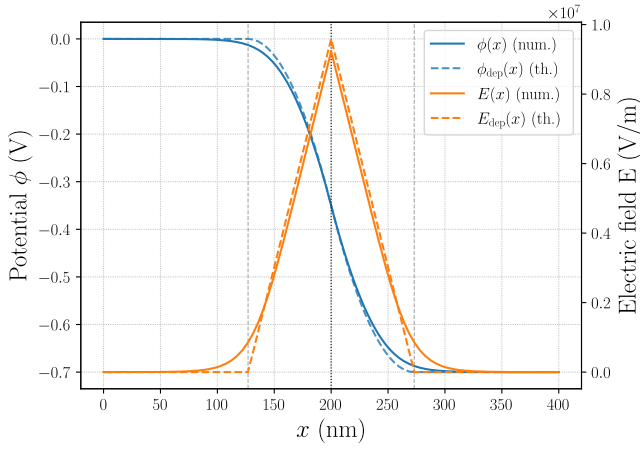


FIG. 7. Electrostatic potential and electric field in the p - n junction. Solid lines show the numerical drift–diffusion solution $\phi(x)$ and $E(x)$; dashed lines show the analytical depletion–approximation profiles $\phi_{\text{dep}}(x)$ and $E_{\text{dep}}(x)$. The metallurgical junction and depletion boundaries are indicated as in Figure 6. The close agreement demonstrates that the numerical scheme reproduces the classical equilibrium p - n junction solution.

in the range $[0.5, 0.8]$, so that $W_{\text{dep}}^{\text{num}}$ is not sensitive to the precise choice of the threshold.

Using this definition we obtain $W_{\text{dep}}^{\text{num}} \approx 146.4$ nm, with depletion edges at $x \approx 126.8$ nm and $x \approx 273.2$ nm. These values are in excellent agreement with the analytical predictions $x_n^{\text{th}} = x_j - W_n \approx 127.0$ nm and $x_p^{\text{th}} = x_j + W_p \approx 273.0$ nm. The built-in voltage extracted from the numerical potential, $\phi(L) - \phi(0) \approx -0.700$ V, also matches the Shockley formula to within numerical precision.

Figure 6 shows the equilibrium electron and hole profiles together with the piecewise–constant doping densities. The numerically defined depletion region based on the majority–carrier criterion almost coincides with the analytical depletion region. Figure 7 compares the numerical potential and electric field with the depletion–approximation solutions $\phi_{\text{dep}}(x)$ and $E_{\text{dep}}(x)$. The numerical scheme reproduces the textbook p - n junction behavior: a nearly flat potential in the neutral regions, a parabolic potential drop and triangular electric field in the depletion region, and a peak field at the metallurgical junction.

D. Validation against OghmaNano

We benchmark our drift–diffusion solver against OghmaNano for the same multilayer organic device (PNDIT-F3N /D18:L8-BO/PEDOT:PSS) under identical material parameters (see Table II). From the computed J - V curve we extract the standard photovoltaic metrics V_{oc} , J_{sc} , $(V_{\text{mpp}}, J_{\text{mpp}})$, P_{max} , FF and PCE (Table III).

To quantify not only scalar metrics but also the full-curve agreement, we further evaluate curve-level discrep-

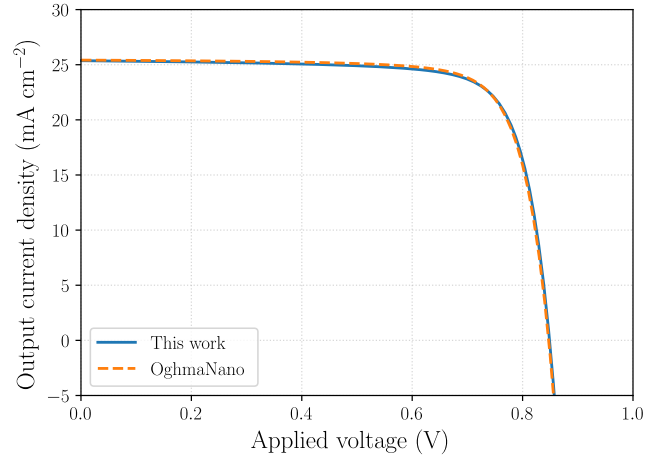


FIG. 8. Comparison of the J - V characteristics between this work and OghmaNano for the PNDIT-F3N/D18:L8-BO/PEDOT:PSS device.

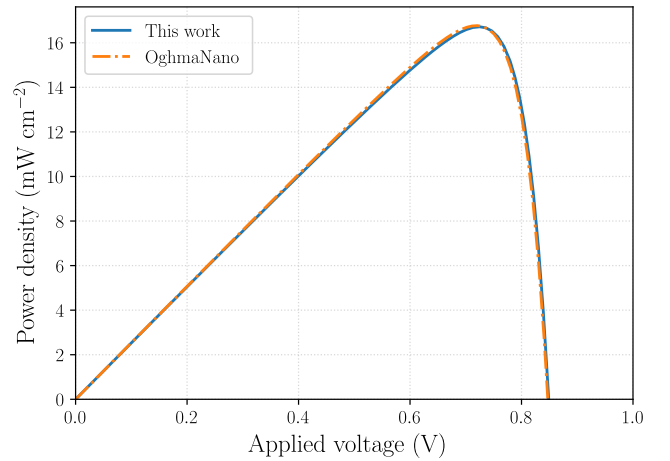


FIG. 9. Comparison of the power-density curves $P(V) = V J_{\text{out}}(V)$ between this work and OghmaNano for the same device and parameter set.

ancies on a common voltage grid $\{V_k\}_{k=1}^N$ and define normalised error measures

$$e_2 = \frac{1}{J_{\text{sc}}^{\text{ref}}} \left(\frac{1}{N} \sum_{k=1}^N (J_{\text{out}}(V_k) - J_{\text{out}}^{\text{ref}}(V_k))^2 \right)^{1/2},$$

$$e_\infty = \frac{1}{J_{\text{sc}}^{\text{ref}}} \max_{1 \leq k \leq N} |J_{\text{out}}(V_k) - J_{\text{out}}^{\text{ref}}(V_k)|. \quad (79)$$

Here “ref” denotes the OghmaNano result and $J_{\text{sc}}^{\text{ref}}$ is used for normalisation. In the present comparison we use $N = 2001$ points and evaluate the errors on $V \in [0, V_{\text{oc}}^{\text{ref}}]$.

Figures 8–9 show that the J - V curve and the power-density curve predicted by this work closely overlap with the OghmaNano reference across the full operating range. Consistently, the extracted photovoltaic metrics in Ta-

TABLE II. Key model parameters for the PNDIT-F3N/D18:L8-BO/PEDOT:PSS organic solar cell used in the OghmaNano benchmark and in this work.

Quantity	Symbol	PNDIT-F3N	D18:L8-BO	PEDOT:PSS	Unit
Layer thickness	d	5	120	20	nm
Relative permittivity	ϵ_r	3.0	3.0	3.0	–
Electron diffusion coefficient	D_n	1.0×10^{-3}	3.9×10^{-9}	1.0×10^{-3}	$\text{m}^2 \text{s}^{-1}$
Hole diffusion coefficient	D_p	1.0×10^{-3}	3.9×10^{-9}	1.0×10^{-3}	$\text{m}^2 \text{s}^{-1}$
Conduction-band DOS	N_c	1.0×10^{26}	1.0×10^{26}	1.0×10^{26}	m^{-3}
Valence-band DOS	N_v	1.0×10^{26}	1.0×10^{26}	1.0×10^{26}	m^{-3}
Electron affinity	Φ_{EA}	–4.2	–4.2	–4.2	eV
Ionisation potential	Φ_{IP}	–5.48	–5.48	–5.48	eV
Equilibrium Fermi level	E_{F0}	–4.245	–4.84	–5.435	eV
Bulk bimolecular recomb.	β	0	1.7×10^{-17}	0	$\text{m}^3 \text{s}^{-1}$
Uniform generation rate	G	0	1.358×10^{28}	0	$\text{m}^{-3} \text{s}^{-1}$
Left boundary electron recomb. velocity	$v_{n,l}$	1.0×10^5	–	–	$\text{m}^2 \text{s}^{-1}$
Left boundary hole recomb. velocity	$v_{p,l}$	1.0×10^5	–	–	$\text{m}^2 \text{s}^{-1}$
Right boundary electron recomb. velocity	$v_{n,r}$	–	–	1.0×10^5	$\text{m}^2 \text{s}^{-1}$
Right boundary hole recomb. velocity	$v_{p,r}$	–	–	1.0×10^5	$\text{m}^2 \text{s}^{-1}$

TABLE III. Extracted photovoltaic metrics from the J - V curves: this work vs OghmaNano.

	V_{oc} (V)	J_{sc} (mA/cm^2)	V_{mpp} (V)	J_{mpp} (mA/cm^2)	P_{max} (mW/cm^2)	FF	PCE (%)
This work	0.848768843	25.36517	0.7246364	23.07191831	16.71875182	0.776562772	16.71875182
OghmaNano	0.847151225	25.41794	0.7198667	23.29781475	16.77132226	0.778871855	16.77132226

ble III differ by less than 1% for all reported quantities, with a mean absolute relative deviation of about 0.42%. The curve-level errors provide a stricter, pointwise assessment: for the J - V curve we obtain $e_2 = 9.22 \times 10^{-3}$ and $e_\infty = 3.57 \times 10^{-2}$, while for the power-density curve we obtain $e_2 = 1.01 \times 10^{-2}$ and $e_\infty = 4.56 \times 10^{-2}$. The RMS discrepancies are therefore at the $\sim 1\%$ level, and the maximum pointwise discrepancies remain below $\sim 5\%$, which is compatible with the small differences observed in the scalar device metrics. These results provide an independent validation that our discretisation (finite-volume flux evaluation and boundary-condition implementation) and numerical solution strategy reproduce a trusted reference solver, supporting the accuracy and reliability of the proposed model for multilayer organic solar-cell simulations.

E. Exciton dynamics

To demonstrate the capability of the numerical framework in handling complex kinetic processes, we implemented a zero-dimensional (0D) exciton dynamics model [7] to simulate the transient evolution of localized exciton (LE) and charge-transfer (CT) states as well as charge separated (CS) states in organic solar cells. The model is based on the rate equations described by Eqs.(43)–(44), depicting the generation, transfer, recombination, and dissociation processes of LE, CT and CS states through coupling with drift-diffusion-poisson equations.

To evaluate the decay kinetics of the different species,

we apply a 1 ps square light pulse (0–1 ps) under open-circuit conditions. All kinetic parameters are taken from Table IV and are constrained to satisfy detailed balance, ensuring a thermodynamically self-consistent parameter set. Figure 10 presents the transient responses of the normalized [LE], [CT], and the free-carrier densities n and p at the midpoint of the active layer, plotted versus time on a logarithmic axis. Upon illumination, [LE] rises first, indicating that photogeneration initially populates local excitons. After the pulse is switched off at $t_{\text{off}} = 1\text{ps}$, [LE] decays while [CT] continues to rise, indicating ongoing LE \rightarrow CT conversion. At later times, [CT] also starts to decay, whereas the free-carrier densities n and p build up and subsequently decay due to recombination. The sequential rise and decay of LE, CT, and CS population indicates the dynamic interaction between those states following the state diagram in Figure 3. The results demonstrate that the proposed numerical framework can capture exciton dynamics relevant to excitonic photovoltaics, particularly organic solar cells.

F. Transient current decay

Referring to [20], we designed a voltage scan protocol as

$$V_{\text{app}} = V_{\text{bi}} \left[1 - \frac{\tanh(\chi t)}{\tanh(\chi t_f)} \right], \quad \text{with } \chi = 0.1, t_f = 10^4, \quad (80)$$

TABLE IV. Key parameters for the 0-D exciton kinetic model coupled with drift-diffusion-poisson system.

Quantity	Symbol	ETL	Active Layer	HTL	Unit
Layer thickness	d	100	100	100	nm
Relative permittivity	ϵ_r	3.0	3.0	3.0	–
Electron diffusion coefficient	D_n	7.7×10^{-5}	7.7×10^{-6}	7.7×10^{-9}	$\text{m}^2 \text{s}^{-1}$
Hole diffusion coefficient	D_p	7.7×10^{-9}	7.7×10^{-6}	7.7×10^{-5}	$\text{m}^2 \text{s}^{-1}$
Conduction-band eDOS	N_c	2×10^{25}	2×10^{25}	2×10^{25}	m^{-3}
Valence-band eDOS	N_v	2×10^{25}	2×10^{25}	2×10^{25}	m^{-3}
Effective density of states for LE	g_{LE}	–	8×10^{25}	–	m^{-3}
Effective density of states for CT	g_{CT}	–	4×10^{25}	–	m^{-3}
Free energy difference for CT	ΔG_{CT}	–	1.31	–	eV
Free energy difference between LE and CT state	$\Delta G_{LE,CT}$	–	0.32	–	eV
Free energy difference between CT and CS state	$\Delta G_{CT,CS}$	–	0.12	–	eV
Electron affinity	Φ_{EA}	0.0	0.0	0.0	eV
Ionisation potential	Φ_{IP}	–1.19	–1.19	–1.19	eV
Equilibrium Fermi level	E_{F0}	–0.1	–0.595	–1.09	eV
LE→CT transfer rate	$k_{LE \rightarrow CT}^{\text{trans}}$	–	1.7×10^{11}	–	s^{-1}
CT→LE transfer rate	$k_{CT \rightarrow LE}^{\text{trans}}$	–	1×10^9	–	s^{-1}
LE recombination rate	k_{LE}^{rec}	–	5.39×10^9	–	s^{-1}
CT recombination rate	k_{CT}^{rec}	–	7×10^9	–	s^{-1}
CT dissociation rate	$k_{CT \rightarrow CS}^{\text{diss}}$	–	2×10^{10}	–	s^{-1}
Free charge to CT state rate constant	$B_{CS \rightarrow CT}^{\text{for}}$	–	7.4×10^{-16}	–	$\text{m}^3 \text{s}^{-1}$
Equilibrium LE concentration	$[LE]_0$	–	3.3×10^{-2}	–	m^{-3}
Equilibrium CT concentration	$[CT]_0$	–	5.6×10^1	–	m^{-3}
Laser generation rate	G	0	1.1×10^{29}	0	$\text{m}^{-3} \text{s}^{-1}$
Left boundary electron recomb. velocity	$v_{n,l}$	1.0×10^5	–	–	$\text{m}^2 \text{s}^{-1}$
Left boundary hole recomb. velocity	$v_{p,l}$	10	–	–	$\text{m}^2 \text{s}^{-1}$
Right boundary electron recomb. velocity	$v_{n,r}$	–	–	10	$\text{m}^2 \text{s}^{-1}$
Right boundary hole recomb. velocity	$v_{p,r}$	–	–	1.0×10^5	$\text{m}^2 \text{s}^{-1}$

and assume monomolecular recombination (depending solely on the local hole concentration p) alone

$$R(n, p) = \gamma p, \quad (81)$$

taking $\gamma = 1500$ (same magnitude as reference) to simulate a transient current behavior. And the total current calculated by

$$\mathbf{J} = \mathbf{J}_n + \mathbf{J}_p + \mathbf{J}_P + \mathbf{J}_d, \quad (82)$$

where $\mathbf{J}_d = \frac{\partial E}{\partial t}$ is displacement current.

Figure 11 shows the total current density $\mathbf{J}(t)$ as a function of the dimensional time t (in seconds). The main panel illustrates the slow relaxation of the current

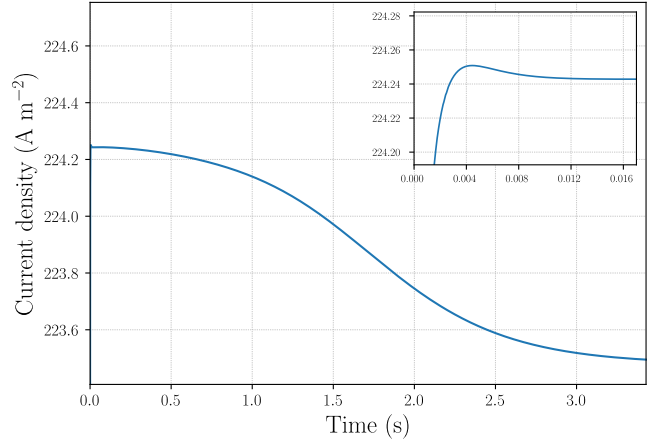


FIG. 11. Current density versus time at left boundary response under a fast decay voltage scan protocol.

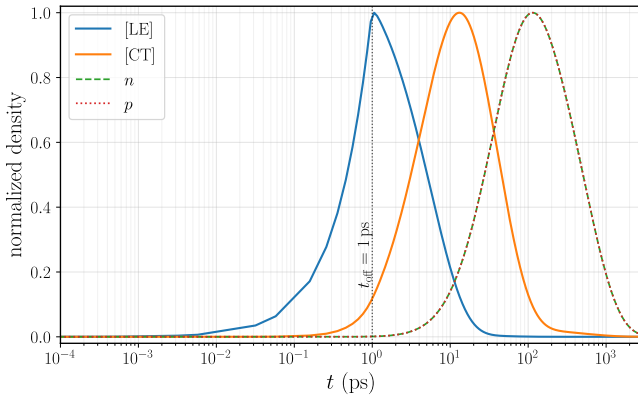


FIG. 10. Transient response for normalized [LE], [CT], and free carriers at the active-layer midpoint under a 0–1 ps light pulse.

towards its steady value over a macroscopic time interval of a few seconds, while the inset zooms into the initial short-time window and reveals a rapid overshoot followed by a monotone decay. Although the time axis used here differs from that in [20], the overall transient behaviour closely resembles their Figure 7. In particular, our computation clearly resolves the fast electronic transient that is not present in the asymptotic approximation of [32], demonstrating that the proposed time-integration scheme can accurately capture such short-time-scale dynamics.

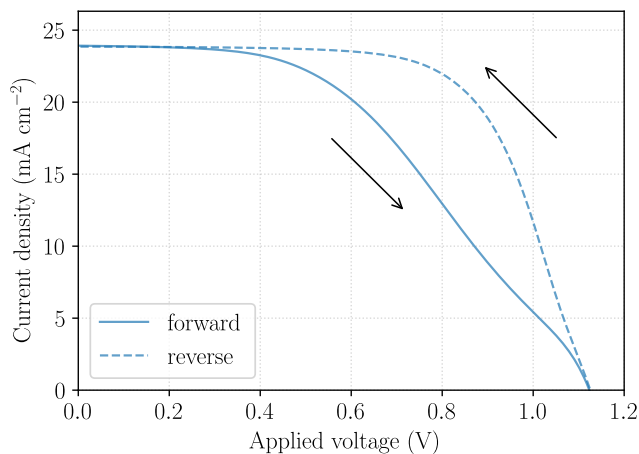


FIG. 12. Simulated current–voltage characteristics of a three-layer perovskite solar cell with mobile ions at a scan rate of 0.1 V s^{-1} . The device consists of an electron-transport layer (ETL, 100 nm), a perovskite absorber (600 nm) and a hole-transport layer (HTL, 200 nm). Mobile ionic vacancies are included only in the perovskite layer. Solid and dashed lines denote forward ($0 \rightarrow 1.2 \text{ V}$) and reverse ($1.2 \rightarrow 0 \text{ V}$) scans, respectively; the black arrows indicate the corresponding scan directions. A clear J – V hysteresis loop is obtained within the same drift–diffusion–Poisson framework.

G. J – V hysteresis in perovskite solar cell with mobile ions

Using the parameter set in Table V, we simulate a three-layer perovskite solar cell with mobile ionic vacancies in the absorber. The optical generation is treated as uniform in the perovskite layer with a volume generation rate $G = 2.5 \times 10^{27} \text{ m}^{-3} \text{ s}^{-1}$, which yields a short-circuit current density $J_{\text{sc}} \approx 22 \text{ mA cm}^{-2}$, comparable to experimentally reported values for high-performance perovskite devices. Ionic vacancies with density $N_0 = 1.6 \times 10^{25} \text{ m}^{-3}$ and diffusion coefficient $D_I = 10^{-17} \text{ m}^2 \text{ s}^{-1}$ are included only in the perovskite layer, while the transport layers are assumed ion-immobile.

Figure 12 shows the resulting J – V characteristics under a voltage scan from 0 to 1.2 V and back at a scan rate of 0.1 V s^{-1} . The forward and reverse sweeps display a pronounced hysteresis loop: during the forward scan the current density decreases smoothly from J_{sc} to the vicinity of the open-circuit voltage, whereas the reverse scan exhibits a much steeper rise in current and a delayed recovery near $V \approx 1 \text{ V}$. This behavior is entirely captured by the coupled drift–diffusion–Poisson–ionic transport model without any additional empirical hysteresis terms.

The hysteresis originates from the slow redistribution of mobile ions, which gradually screens the internal electric field and modifies the band bending at the ETL/perovskite and perovskite/HTL interfaces. Under forward bias, ions move in a direction that partially counteracts the built-in field, reducing charge extraction and leading to lower current. When the scan direction is re-

versed, the ionic configuration lags behind the applied voltage, so that the internal field is temporarily closer to its initial state, resulting in a higher current for the same applied voltage.

V. CONCLUSION

We have developed and validated a one-dimensional transient drift-diffusion solver for multilayer solar cells that combines a finite-volume discretization with Scharfetter–Gummel-type fluxes and a fifth-order Radau IIA implicit Runge–Kutta scheme for time integration. The spatial discretization enforces local charge conservation on general non-uniform meshes, handles sharp heterojunctions and strongly varying material parameters in a natural way, and is compatible with both density-based and potential-based formulations of the van Roosbroeck system. The temporal discretization, implemented via a modified Radau solver for index-1 DAEs, provides high-order accuracy and robust L-stable damping of fast modes, which is crucial for resolving electronic and ionic dynamics over many orders of magnitude in time.

Systematic convergence studies confirm that the proposed method attains second-order accuracy in space and fifth-order accuracy in time for the coupled Poisson and carrier-continuity equations. In an abrupt p – n junction test, the numerical solution reproduces the classical depletion approximation, including the built-in voltage and depletion widths, within numerical precision. A transient test based on a fast voltage-decay protocol shows that the scheme accurately captures both the rapid initial electronic transient and the subsequent slow relaxation, in quantitative and qualitative agreement with previously reported asymptotic and numerical results. Furthermore, benchmarking against the established simulator OghmaNano for a multilayer organic solar cell shows close agreement in the steady-state J – V response and the extracted photovoltaic metrics. The remaining differences are small (below 1% RMS at the curve level), confirming the accuracy and reliability of our implementation for complex device structure.

To demonstrate both the extensibility of the framework and its physical consistency, we include additional dynamic processes that are important in emerging photovoltaic technologies. In organic solar cells, LE/CT state kinetics are coupled to the drift–diffusion transport equations through local generation and recombination terms, following Azzouzi et al. [7]. This coupling allows the model to resolve exciton dynamics across multiple time scales, from picoseconds to nanoseconds. In perovskite solar cells, mobile ionic vacancies in the absorber are treated with a drift–diffusion equation driven by the Poisson electric field, which naturally produces J – V hysteresis under voltage scans without introducing empirical hysteresis terms and thereby reproduces a key experimental signature. In both extensions, the added equations are nondimensionalized and discretized in the same manner

TABLE V. Key model parameters for the three-layer perovskite solar cell.

Quantity	Symbol	ETL	Perovskite	HTL	Unit
Layer thickness	d	100	600	200	nm
Relative permittivity	ϵ_r	10.0	24.1	3.0	–
Electron diffusion coefficient	D_n	1.0×10^{-5}	1.7×10^{-4}	1.0×10^{-6}	$\text{m}^2 \text{s}^{-1}$
Hole diffusion coefficient	D_p	1.0×10^{-5}	1.7×10^{-4}	1.0×10^{-6}	$\text{m}^2 \text{s}^{-1}$
Conduction-band DOS	N_c	5.0×10^{25}	8.1×10^{24}	5.0×10^{25}	m^{-3}
Valence-band DOS	N_v	5.0×10^{25}	5.8×10^{24}	5.0×10^{25}	m^{-3}
Electron affinity	Φ_{EA}	–4.0	–3.7	–3.1	eV
Ionisation potential	Φ_{IP}	–6.0	–5.4	–5.1	eV
Equilibrium Fermi level	E_{F0}	–4.1	–4.55	–5.0	eV
Trap energy level	E_{trap}	–4.25	–4.55	–4.75	eV
SRH lifetime (electrons)	τ_n	–	3.0×10^{-9}	–	s
SRH lifetime (holes)	τ_p	–	3.0×10^{-9}	–	s
Bulk bimolecular recomb.	β	0	1.0×10^{-18}	0	$\text{m}^3 \text{s}^{-1}$
Ionic vacancy density	N_I	–	1.6×10^{25}	–	m^{-3}
Ionic diffusion coefficient	D_I	0	1.0×10^{-17}	0	$\text{m}^2 \text{s}^{-1}$
Uniform generation rate	G	0	2.5×10^{27}	0	$\text{m}^{-3} \text{s}^{-1}$
Left boundary electron recomb. velocity	$v_{n,l}$	1.0×10^5	–	–	$\text{m}^2 \text{s}^{-1}$
Left boundary hole recomb. velocity	$v_{p,l}$	10	–	–	$\text{m}^2 \text{s}^{-1}$
Right boundary electron recomb. velocity	$v_{n,r}$	–	–	10	$\text{m}^2 \text{s}^{-1}$
Right boundary hole recomb. velocity	$v_{p,r}$	–	–	1.0×10^5	$\text{m}^2 \text{s}^{-1}$

as the core drift–diffusion system, and time integration is carried out with the same high-order Radau IIA scheme.

Compared with existing DD simulators such as IonMonger, Driftfusion, SolarDesign, and SIMsalabim, the present work emphasizes a combination of structure-preserving finite-volume discretization, high-order stiff time integration, and algorithmic transparency. Spatial fluxes are tailored to drift–diffusion transport rather than inherited from generic finite-difference or FEM backends, and time stepping is implemented explicitly rather than delegated to a black-box multistep solver. This design facilitates the analysis and control of numerical errors, the reuse of Jacobians and preconditioners across stages and steps, and the modular extension of the code to new physical sub-models.

Several extensions of the present study are possible. On the modeling side, the one-dimensional framework can be coupled to more detailed optical models, interface-specific recombination schemes, and degradation mechanisms, or generalized to two-dimensional device geometries. On the numerical side, future work could explore tailored

preconditioners and block-structured linear solvers for the coupled stage systems, as well as adaptive strategies that balance spatial, temporal, and algebraic errors in a more systematic way. Nevertheless, the results presented here already indicate that combining finite-volume SG discretizations with high-order Radau IIA time stepping provides a promising and practical route to accurate, robust, and extensible drift–diffusion simulations for advanced solar-cell architectures.

Acknowledgements. J.Y. acknowledges funding support from National Natural Science Foundation of China (No. 62574175 and No. 62404191), Guangdong Basic and Applied Basic Research Foundation (No. 2023A1515111140 and No. 2024A1515012318), Guangdong Provincial Program (No. 2023QN10C144), Shenzhen Science and Technology Program (No. KQTD20240729102028011 and No. JCYJ20240813113553067), and Guangdong Basic Research Center of Excellence for Aggregate Science.

Data availability. The data are available from the authors upon reasonable request.

-
- [1] J. Nelson, *The physics of solar cells* (World Scientific Publishing Company, 2003).
- [2] P. Calado, A. M. Telford, D. Bryant, X. Li, J. Nelson, B. C. O’Regan, and P. R. Barnes, Evidence for ion migration in hybrid perovskite solar cells with minimal hysteresis, *Nature communications* **7**, 13831 (2016).
- [3] W. Van Roosbroeck, Theory of the flow of electrons and holes in germanium and other semiconductors, *The Bell System Technical Journal* **29**, 560 (1950).
- [4] P. Farrell, N. Rotundo, D. H. Doan, M. Kantner, J. Fuhrmann, and T. Koprucki, Drift-diffusion models, in *Handbook of optoelectronic device modeling and simulation* (CRC Press, 2017) pp. 733–772.
- [5] D. Scharfetter and H. Gummel, Large-signal analysis of a silicon read diode oscillator, *IEEE Transactions on Electron Devices* **16**, 64 (1969).
- [6] D. Abdel, P. Vágner, J. Fuhrmann, and P. Farrell, Modelling charge transport in perovskite solar cells: Potential-based and limiting ion depletion, *Electrochimica Acta* **390**, 138696 (2021).
- [7] M. Azzouzi, N. P. Gallop, F. Eisner, J. Yan, X. Zheng, H. Cha, Q. He, Z. Fei, M. Heeney, A. A. Bakulin, *et al.*, Reconciling models of interfacial state kinetics and device performance in organic solar cells: impact of the energy offsets on the power conversion efficiency, *Energy & Environmental Science* **15**, 1256 (2022).
- [8] N. E. Courtier, J. M. Cave, A. B. Walker, G. Richardson, and J. M. Foster, Ionmonger: a free and fast planar perovskite solar cell simulator with coupled ion vacancy and charge carrier dynamics, *Journal of Computational*

- Electronics **18**, 1435 (2019).
- [9] W. Clarke, L. J. Bennett, Y. Grudeva, J. M. Foster, G. Richardson, and N. E. Courtier, Ionmonger 2.0: software for free, fast and versatile simulation of current, voltage and impedance response of planar perovskite solar cells, *Journal of Computational Electronics* **22**, 364 (2023).
- [10] P. Calado, I. Gelmetti, B. Hilton, M. Azzouzi, J. Nelson, and P. R. Barnes, Drifffusion: an open source code for simulating ordered semiconductor devices with mixed ionic-electronic conducting materials in one dimension, *Journal of Computational Electronics* **21**, 960 (2022).
- [11] E. Wei, X. Wang, W. Chen, Y. Fu, L. Zhang, L. Tian, M. Lin, S. Jiao, T. Xu, T. Sun, *et al.*, Solardesign: An online photovoltaic device simulation and design platform, *Chinese Physics B* **34**, 018801 (2025).
- [12] M. Koopmans, V. M. Le Corre, and L. J. A. Koster, Simalabim: An open-source drift-diffusion simulator for semiconductor devices, *Journal of Open Source Software* **7**, 3727 (2022).
- [13] B. Ruhstaller, T. Flatz, D. Rezzonico, M. Moos, N. Reinke, E. Huber, R. Häusermann, and B. Perucco, Comprehensive simulation of light-emitting and light-harvesting organic devices, in *Organic Light Emitting Materials and Devices XII*, Vol. 7051 (SPIE, 2008) pp. 86–97.
- [14] R. Häusermann, E. Knapp, M. Moos, N. A. Reinke, T. Flatz, and B. Ruhstaller, Coupled optoelectronic simulation of organic bulk-heterojunction solar cells: Parameter extraction and sensitivity analysis, *Journal of Applied Physics* **106** (2009).
- [15] R. C. MacKenzie, C. G. Shuttle, M. L. Chabinye, and J. Nelson, Extracting microscopic device parameters from transient photocurrent measurements of p3ht: Pcbm solar cells, *Advanced Energy Materials* **2**, 662 (2012).
- [16] L. F. Shampine and M. W. Reichelt, The matlab ode suite, *SIAM journal on scientific computing* **18**, 1 (1997).
- [17] E. Hairer and G. Wanner, Stiff differential equations solved by radau methods, *Journal of Computational and Applied Mathematics* **111**, 93 (1999).
- [18] J. Blakemore, Approximations for fermi-dirac integrals, especially the function $f_{12}(\eta)$ used to describe electron density in a semiconductor, *Solid-State Electronics* **25**, 1067 (1982).
- [19] L. F. Shampine, Solving $0 = f(t, y(t), y'(t))$ in MATLAB, *J. Numer. Math.* **10**, 291 (2002).
- [20] N. E. Courtier, G. Richardson, and J. M. Foster, A fast and robust numerical scheme for solving models of charge carrier transport and ion vacancy motion in perovskite solar cells, *Applied Mathematical Modelling* **63**, 329 (2018).
- [21] A. Singer, D. Gillespie, J. Norbury, and R. Eisenberg, Singular perturbation analysis of the steady-state poisson–nernst–planck system: Applications to ion channels, *European journal of applied mathematics* **19**, 541 (2008).
- [22] D. He and K. Pan, An energy preserving finite difference scheme for the poisson–nernst–planck system, *Applied Mathematics and Computation* **287**, 214 (2016).
- [23] K. V. Cartwright, Simpson’s rule cumulative integration with ms excel and irregularly-spaced data, *J. Math. Sci. Math. Educ* **12**, 1 (2017).
- [24] A. Il’In, A difference scheme for a differential equation with a small parameter multiplying the second derivative, *Mat. zametki* **6**, 237 (1969).
- [25] D. De G. Allen and R. Southwell, Relaxation methods applied to determine the motion, in two dimensions, of a viscous fluid past a fixed cylinder, *The Quarterly Journal of Mechanics and Applied Mathematics* **8**, 129 (1955).
- [26] A. de Mari, An accurate numerical one-dimensional solution of the p-n junction under arbitrary transient conditions, *Solid-State Electronics* **11**, 1021 (1968).
- [27] P. Virtanen, R. Gommers, T. E. Oliphant, M. Haberland, T. Reddy, D. Cournapeau, E. Burovski, P. Peterson, W. Weckesser, J. Bright, S. J. van der Walt, M. Brett, J. Wilson, K. J. Millman, N. Mayorov, A. R. J. Nelson, E. Jones, R. Kern, E. Larson, C. J. Carey, Í. Polat, Y. Feng, E. W. Moore, J. VanderPlas, D. Laxalde, J. Perktold, R. Cimrman, I. Henriksen, E. A. Quintero, C. R. Harris, A. M. Archibald, A. H. Ribeiro, F. Pedregosa, P. van Mulbregt, and SciPy 1.0 Contributors, SciPy 1.0: Fundamental Algorithms for Scientific Computing in Python, *Nature Methods* **17**, 261 (2020).
- [28] E. Hairer, C. Lubich, and M. Roche, *The numerical solution of differential-algebraic systems by Runge-Kutta methods*, Vol. 1409 (Springer, 2006).
- [29] J. C. Butcher, On the implementation of implicit runge-kutta methods, *BIT Numerical Mathematics* **16**, 237 (1976).
- [30] G. Wanner and E. Hairer, *Solving ordinary differential equations II*, Vol. 375 (Springer Berlin Heidelberg New York, 1996).
- [31] A. R. Curtis, M. J. Powell, and J. K. Reid, On the estimation of sparse jacobian matrices, *IMA Journal of Applied Mathematics* **13**, 117 (1974).
- [32] N. E. Courtier, J. M. Foster, S. E. O’KANE, A. B. Walker, and G. Richardson, Systematic derivation of a surface polarisation model for planar perovskite solar cells, *European Journal of Applied Mathematics* **30**, 427 (2019).